



Structural/functional studies of Trio provide insights into its configuration and show that conserved linker elements enhance its activity for Rac1

Received for publication, December 13, 2021, and in revised form, June 21, 2022. Published, Papers in Press, June 30, 2022.

<https://doi.org/10.1016/j.jbc.2022.102209>

Sumit J. Bandekar^{1,2}, Chun-Liang Chen³, Sandeep K. Ravala³, Jennifer N. Cash⁴ , Larisa V. Avramova³, Mariya V. Zhalnina³, J. Silvio Gutkind⁵, Sheng Li⁶, and John J. G. Tesmer^{3,*}

From the ¹Department of Medicinal Chemistry, and ²Life Sciences Institute, University of Michigan, Ann Arbor, Michigan, USA; ³Departments of Biological Sciences and of Medicinal Chemistry and Molecular Pharmacology, Purdue University, West Lafayette, Indiana, USA; ⁴Department of Molecular and Cellular Biology, University of California-Davis, Davis, California, USA; ⁵Department of Pharmacology and Moores Cancer Center, University of California, San Diego, San Diego, California, USA; ⁶Department of Medicine, University of California San Diego, La Jolla, California, USA

Edited by Henrik Dohlman

Trio is a large and highly conserved metazoan signaling scaffold that contains two Dbl family guanine nucleotide exchange factor (GEF) modules, TrioN and TrioC, selective for Rac and RhoA GTPases, respectively. The GEF activities of TrioN and TrioC are implicated in several cancers, especially uveal melanoma. However, little is known about how these modules operate in the context of larger fragments of Trio. Here we show *via* negative stain electron microscopy that the N-terminal region of Trio is extended and could thus serve as a rigid spacer between the N-terminal putative lipid-binding domain and TrioN, whereas the C-terminal half of Trio seems globular. We found that regions C-terminal to TrioN enhance its Rac1 GEF activity and thus could play a regulatory role. We went on to characterize a minimal, well-behaved Trio fragment with enhanced activity, Trio_{1284–1959}, in complex with Rac1 using cryo-electron microscopy and hydrogen-deuterium exchange mass spectrometry and found that the region conferring enhanced activity is disordered. Deletion of two different strongly conserved motifs in this region eliminated this enhancement, suggesting that they form transient intramolecular interactions that promote GEF activity. Because Dbl family RhoGEF modules have been challenging to directly target with small molecules, characterization of accessory Trio domains such as these may provide alternate routes for the development of therapeutics that inhibit Trio activity in human cancer.

Rho family guanine nucleotide exchange factors (RhoGEFs) (1) activate small guanosine triphosphatases (GTPases) of the Rho family (2), thereby regulating cell growth *via* transcriptional events and motility *via* modulation of the actin cytoskeleton. RhoGEF dysregulation is well known to lead to oncogenic phenotypes including growth, migration, and metastasis (3, 4). Trio (ARHGEP23) is an unusual member of the Dbl family of RhoGEFs in that it contains two catalytic

RhoGEF modules (Fig. 1A) (5). Both RhoGEF activities of Trio are crucial to the growth and metastatic spread of uveal melanoma (6, 7), a particularly fatal cancer once it metastasizes to the liver and one with no effective therapeutics available (8, 9). In tumor xenograft models of metastatic uveal melanoma, knockdown of Trio is effective at reducing tumor size and weight, suggesting inhibitor molecules targeting Trio activity could serve as effective therapeutics (7). Trio can also be involved in adult T-cell leukemia (10) and is overexpressed in a variety of other cancers (7), leading to broad interest in targeting this protein.

Dbl family GEF modules are composed of a Dbl homology (DH) domain that binds Rho GTPases followed by a regulatory pleckstrin homology (PH) domain. The N-terminal GEF module of Trio (TrioN) catalyzes nucleotide exchange on Rac subfamily members, whereas the C-terminal module (TrioC) catalyzes nucleotide exchange on RhoA subfamily members (5). Both TrioN and TrioC have been characterized structurally and functionally as standalone modules (11–13), and prior screening efforts have tried to identify molecules that target TrioC (14–16), but none have succeeded past *in vitro* studies. Understanding how the accessory regions and/or domains of Trio contribute to GEF activity may provide alternative therapeutic routes by which to modulate Trio function.

Most RhoGEFs are large, multidomain proteins, and in other RhoGEFs, accessory regions have been shown to positively or negatively regulate GEF activity. For example, p115-RhoGEF, PDZ-RhoGEF, and leukemia-associated RhoGEF are demarked by a regulator of G protein signaling homology domain that interacts with the heterotrimeric G protein G $\alpha_{12/13}$ to positively regulate GEF activity in cells (17), whereas Asef, collybistin, and ephexin all contain adjacent SH3 domains that negatively regulate GEF activity (18–20). The functions of the accessory domains in Trio are primarily inferred by the roles of homologous domains in other proteins. The N-terminal Cral/Trio (CT) domain (Fig. 1) is homologous to Sec14 lipid transferase domains, which bind phosphoinositides or hydrophobic ligands (21, 22). One report further suggested that Dbl

* For correspondence: John J. G. Tesmer, jtesmer@purdue.edu.

Structure/function studies of human Trio

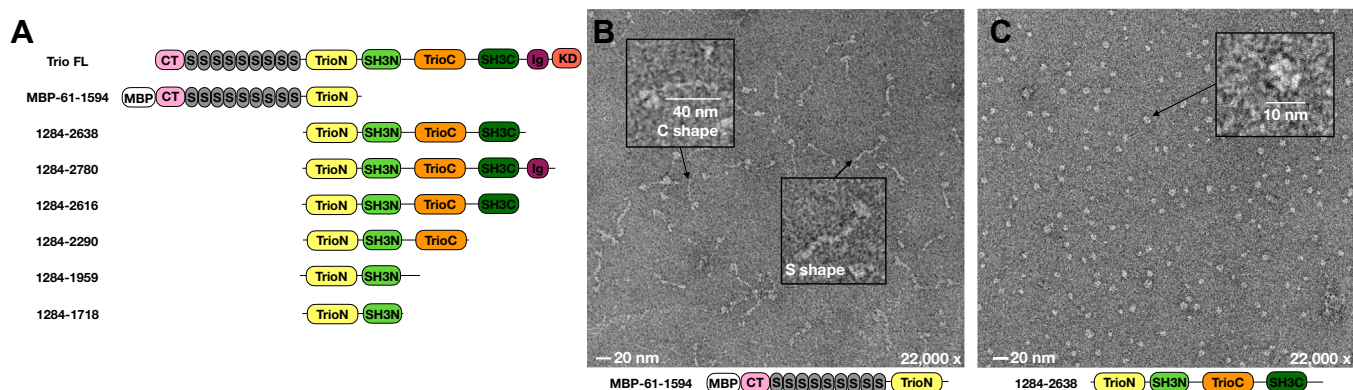


Figure 1. Negative stain EM reveals low-resolution features of different regions of Trio. A, domain architecture of human Trio and variants used in this work. Domains are abbreviated as CT, Cral/Trio; S, spectrin repeat; TrioN, N-terminal GEF module; SH3N, N-terminal Src homology 3 domain; TrioC, C-terminal GEF module; SH3C, C-terminal Src homology 3 domain; Ig, immunoglobulin-like domain; KD, kinase domain; MBP, maltose binding protein. B, representative micrographs show that the N-terminal domains of Trio adopt an extended configuration, whereas the central region of Trio is condensed (C). Insets: representative particles with length estimates. EM, electron microscopy; GEF, guanine nucleotide exchange factor.

family CT domains could serve as a binding site for the G protein $\beta\gamma$ ($G_{\beta\gamma}$) heterodimer (23). The CT domain is followed by nine spectrin repeats (S1-S9), which are extended 3-helix bundles found in many proteins associated with the actin cytoskeleton and expected to serve a structural role (24). The TrioN GEF module is followed by a N-terminal Src homology 3 domain (SH3N), which canonically binds to proline-rich sequences containing the motif PXXP (25), as it does in Kalirin, a close homolog of Trio (26). Next is the TrioC module followed by another SH3 domain (C-terminal Src homology 3 [SH3C]). The next domain is an Ig-like domain that one report concluded binds to activated RhoA and thereby contributes to the localization of Trio on the plasma membrane (27). Trio ends with a protein kinase domain that belongs to the Ca^{2+} -calmodulin kinase subfamily followed by an autoinhibitory C-terminal helical signature that interacts with Ca^{2+} -calmodulin in functional members of the family. However, activity for the Trio kinase domain has yet to be reported.

Aside from the isolated functions of the individual Trio domains, it is also important to study how they function in context of the full-length protein. A region encompassing the spectrin repeats, TrioN GEF module, and SH3N domain has been shown as the minimal region of Trio necessary to stimulate neurite outgrowth in cells (28). In addition, the heterotrimeric G protein G_{α_q} has been shown to directly bind to the TrioC GEF module and stimulate RhoA exchange by relieving intramolecular autoinhibition within the TrioC module (13, 29–31). However, in cells where full-length Trio is present, G_{α_q} stimulates both TrioN and TrioC GEF activity (6, 7). It is unknown whether G_{α_q} signaling leads to activation of the TrioN module by mechanisms other than membrane recruitment.

In this study, we hypothesized that adjacent regions or domains could modulate the activity of the Trio GEF modules in either positive or negative ways, as implied by studies with the Kalirin SH3N domain (26) and be part of a larger regulatory framework controlled by G_{α_q} . To test this theory, we purified various fragments of human Trio and compared their GEF activities, structures, and dynamics. Our negative stain

electron microscopy (EM) data are consistent with the N-terminal half of Trio existing in an extended conformation dominated by the spectrin repeats and the middle of the protein containing both RhoGEF modules and their SH3 domains in a globular configuration, suggesting that these signaling domains and their extended linker regions could be closely associated. Our results are consistent with G_{α_q} regulating TrioC as a standalone module that is not obviously influenced by surrounding regions, but with TrioN being profoundly activated by conserved elements within a disordered region C terminal to the SH3N domain. However, these elements were not ordered in high resolution cryo-EM maps or evidenced in hydrogen-deuterium exchange mass spectrometry (HDX-MS) measurements. Our work thus further illuminates a network of intramolecular and intermolecular protein–protein interactions that underlie regulation in full-length Trio.

Results

Negative stain EM characterization of Trio fragments provides insights into overall architecture of Trio

To capture snapshots of the overall configuration of Trio, we first attempted to purify Trio fragments starting from the N terminus. The largest successfully purified to homogeneity ($Trio_{MBP-61-1594}$) contained the CT domain, nine spectrin repeats, and TrioN. The protein was studied as the maltose binding protein (MBP) fusion because it aggregated when MBP was cleaved. Negative stain EM micrographs revealed an extended particle with ~ 45 nm maximum length (Fig. 1, B and C). The $Trio_{MBP-61-1594}$ particle (Inset, Fig. 1B) has a globular head, likely representing MBP and the CT domain, followed by a thin extended tail region of about 40 nm that likely corresponds to the spectrin repeat region of Trio. A fully extended length of 45 nm is estimated for the repeats from a model containing fully extended nine copies of the spectrin repeat. In comparison, the solution structure of the seven spectrin repeats of plectin is a rod-like structure of 35 nm, which would also correspond to 45 nm if there were nine repeats (32). In Trio, the shorter length may be accounted for by curvature and

flexibility in the spectrin repeats. Some Trio_{MBP-61-1594} particles were for example shaped roughly like an “S” or a “C” (Fig. 1B, insets). The particle heterogeneity indicated that a 3D reconstruction using this N-terminal fragment would be challenging. Because longer Trio fragments starting at the N-terminus could not be purified, we decided to purify fragments beginning at the putative globular domains of Trio, beginning with TrioN (residue 1284). We initially purified and imaged the Trio₁₂₈₄₋₂₆₃₈ fragment, which included TrioN through SH3C (Fig. 1C). Micrographs revealed a globular particle with a diameter of ~10 nm, but this particle did not exhibit any discernible features in 2D averages (Fig. S1). Larger Trio fragments including the Ig and kinase domains did not express. Therefore, we decided to proceed with functional experiments on the central region of Trio containing the catalytic domains and their associated SH3 domains.

Basal and Gα_q-stimulated GEF activity of Trio variants

Using a Förster resonance energy transfer (FRET)-based GEF assay (Fig. S2), we first confirmed that the individual TrioN and TrioC GEF modules activate only their cognate substrates (Rac1 and RhoA, respectively, in our experiments) 3- to 4-fold (Fig. 2A). To test whether the presence of other regions affected this basal GEF activity, we compared the activity of the isolated GEF modules to that of Trio₁₂₈₄₋₂₆₃₈. Trio₁₂₈₄₋₂₆₃₈ had similar GEF activity on RhoA as TrioC in isolation, but 8-fold higher activity on Rac1 than TrioN in isolation (Fig. 2B). Gα_q·GDP·AlF₄⁻ enhanced Trio₁₂₈₄₋₂₆₃₈

RhoA GEF activity to the same extent as TrioC (~2.5-fold) but had no effect on Rac1 exchange activity (Figs. 2B and S3). Therefore, Gα_q seems agnostic to sequences outside the TrioC module. To identify the residues responsible for enhanced Rac1 GEF activity of TrioN, we generated a series of truncations (Fig. 3). These proteins started with residue 1284 at the N terminus of TrioN and ended at residue 1718 (after SH3N), 1959 (after a ~240 residue linker region), 2290 (after TrioC), 2616 (after SH3C), and 2780 (after the Ig domain). Constructs larger than this did not express or behave well. Each variant was tested for activity *versus* TrioN or TrioC in paired experiments (Fig. 3). Constructs ending at residue 1959 or later displayed 3- to 7-fold enhanced GEF activity on Rac1 relative to TrioN alone, with Trio₁₂₈₄₋₂₆₁₆ having the highest rate (Fig. 3A), similar to the rate observed for Trio₁₂₈₄₋₂₆₃₈. All the variants that included the TrioC GEF module had similar activity on RhoA relative to TrioC alone (Fig. 3B).

Cryo-EM analysis of the Trio₁₂₈₄₋₁₉₅₉-Rac1 complex

To gain structural insight into the mechanism of GEF enhancement, we decided to use a single particle cryo-EM approach. We chose Trio₁₂₈₄₋₁₉₅₉ for this analysis because its molecular weight (78 kDa) was potentially large enough to get a high resolution reconstruction and also because it was the most well-behaved and highest yielding Trio variant. Furthermore, it is composed of a relatively simple system of three structural domains (DH, PH, and SH3N), which would facilitate modeling if the resolution of the reconstruction were low. The Trio₁₂₈₄₋

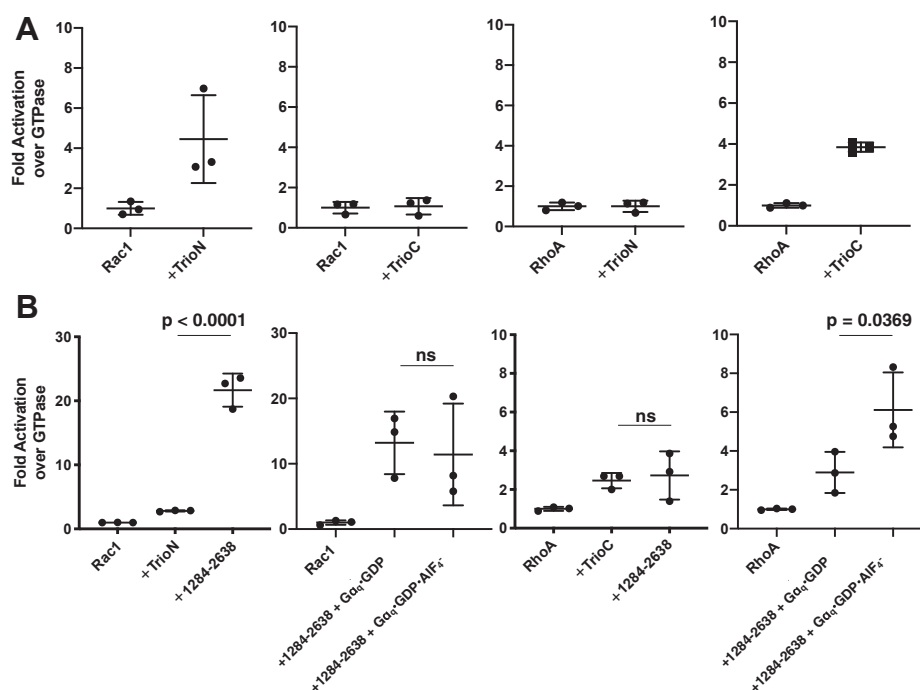


Figure 2. GEF assays show enhanced Rac1 but not RhoA exchange in larger Trio fragments and that Gα_q regulation of TrioC is insensitive to adjacent regions. A, control experiments showing that each Trio GEF module is selective for its given GTPase. B, basal activities of Trio₁₂₈₄₋₂₆₃₈ compared to the isolated GEF modules and Gα_q·GDP·AlF₄⁻ stimulated Trio₁₂₈₄₋₂₆₃₈. In each panel, Rac1 and RhoA exchange activity is shown in the *left* and *right* two plots, respectively. Note that in these assays Gα_q·GDP·AlF₄⁻ activates nucleotide exchange on RhoA but not Rac1. Scatter plots of GEF assays were normalized to rate of GTPase alone, N = 3 experiments in at least duplicate. Error bars indicate standard deviation. *p*-values are from a one-way ANOVA with Dunnett’s correction for multiple comparisons. GEF, guanine nucleotide exchange factor; ns, not significant.

Structure/function studies of human Trio

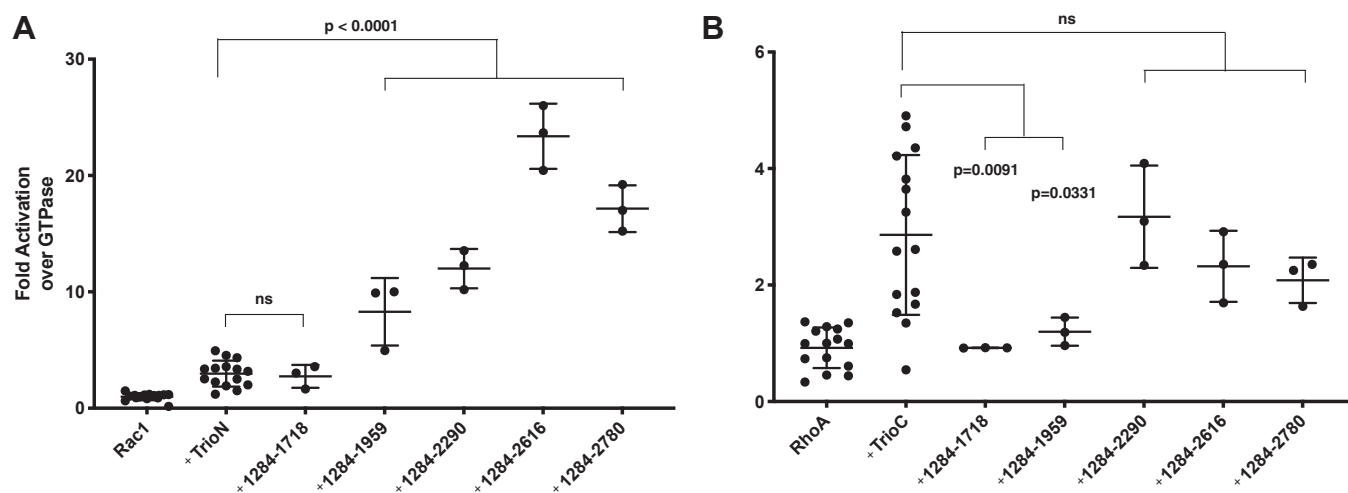


Figure 3. GEF activity data for progressive C-terminal truncations of the middle region of Trio. Panels (A) and (B) depict Rac1 and RhoA exchange experiments, respectively. Box and whisker plots of GEF assays were normalized to rate of GTPase alone (N = 3 experiments in at least duplicate). Error bars indicate standard deviation. *p*-values are from a one-way ANOVA with Dunnett's correction for multiple comparisons. ns, not significant; GEF, guanine nucleotide exchange factor.

1959–Rac1 complex was first profiled by negative stain EM (Fig. S4), yielding particles about 10 nm in diameter that seemed to have better detail than particles of Trio₁₂₈₄₋₂₆₃₈ alone (Fig. S1). Cryo-EM single particle analysis ultimately yielded a 2.9 Å map (Fig. 4), which is unusually high resolution for what

ended up being a ~55 kDa structure (not considering regions that ended up disordered). To fit the map, the crystal structure of the TrioN–Rac1 complex (PDB entry 2NZ8) was placed into the map, then subjected to multiple rounds of model building and real space refinement (Fig. 4, Table 1, and Fig. S5). The final

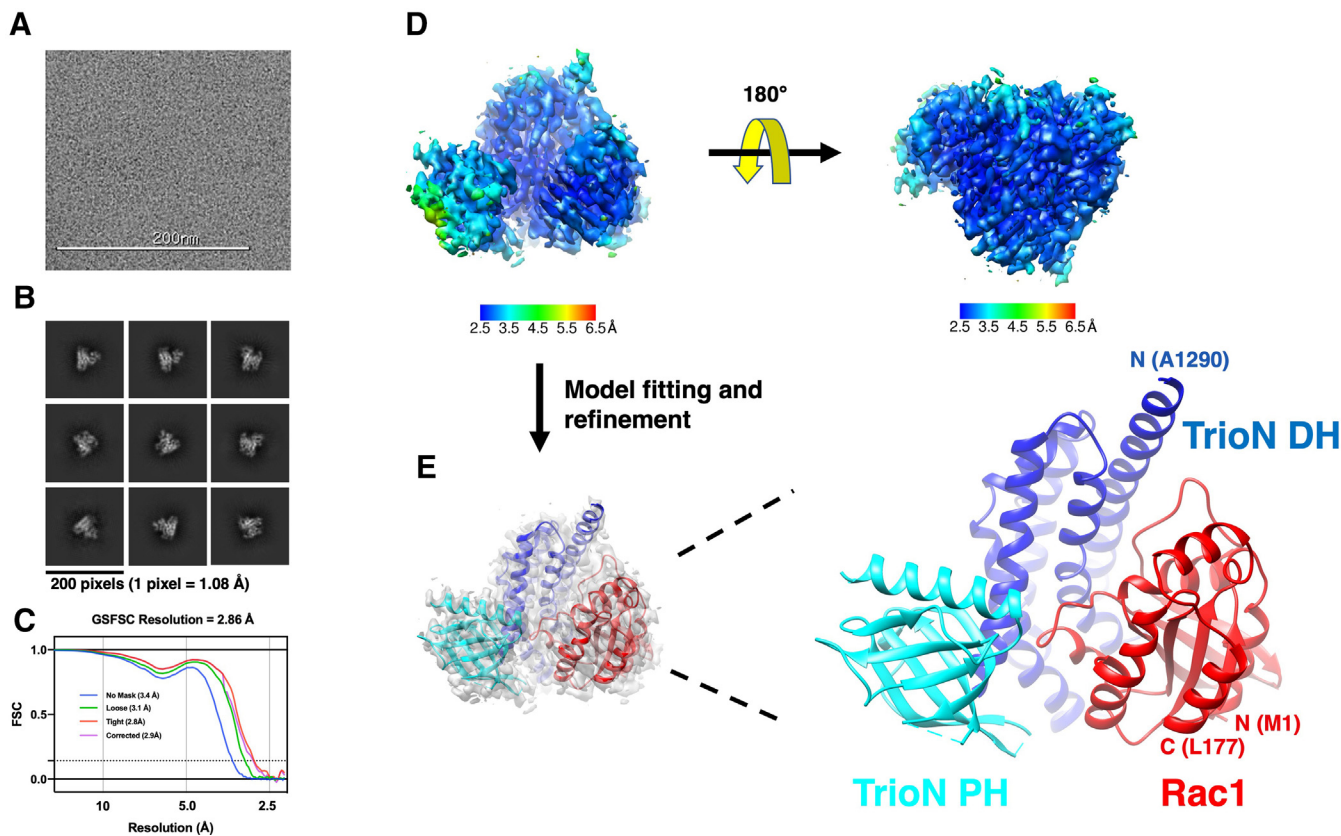


Figure 4. Cryo-EM reconstruction of the Trio₁₂₈₄₋₁₉₅₉–Rac1 complex. A, representative cryo-EM micrograph. B, representative 2D classes. C, resolution estimation of the Trio₁₂₈₄₋₁₉₅₉–Rac1 cryo-EM reconstruction based on the FSC=0.143 criterion with different masking options. D, cryo-EM map of Trio₁₂₈₄₋₁₉₅₉–Rac1. Local resolution of the cryo-EM map was estimated in cryoSPARC. E, model fitting and refinement. A starting model generated from the crystal structure of the TrioN–Rac1 complex (PDB entry 2NZ8) was fit into the cryo-EM density map and then refined using Coot and PHENIX. The DH and PH domains of TrioN are shown in blue and cyan, respectively. Rac1 is shown in red. DH, Dbl homology; EM, electron microscopy; PH, pleckstrin homology.

model contains residues 1 to 177 of Rac1, and residues 1284 to 1594 of Trio. However, there was no obvious density for any domain or residues C terminal to the Trio PH domain. Comparison of the complex, which may be the first of a RhoGEF DH/PH module by single particle cryo-EM, with that of the TrioN–Rac1 crystal structure reveals few differences (Fig. S5). More residues of the PH domain are ordered in the cryo-EM structure, and the domain is rotated about 4° with respect to the DH domain relative to that of the crystal structure. The register of the β 5 strand of the PH domain is different, but the new cryo-EM structure agrees with the register of the model in the crystal structure of TrioN alone (PDB entry 1NTY). Density for the N-terminal helix of the cryo-EM DH domain extends outward by eight additional residues, and residues 26 to 31 in Switch 1 of Rac1 adopt a markedly different conformation. Most of the differences between the models seem to be a consequence of lattice contacts in the 2NZ8 structure, which occur near Switch 1 of Rac1 and at the hinge region of the DH/PH module. Furthermore, if the N-terminus of Trio in 2NZ8 were extended as a helix as far as it is in the cryo-EM structure, it would cause a steric clash with a lattice contact. This suggests that a cryo-EM structure, even at a lower nominal resolution of 2.9 Å, can potentially yield more detail and, perhaps, a more native conformation than a 2 Å crystal structure.

Analysis of the Trio₁₂₈₄₋₁₉₅₉–Rac1 complex by HDX-MS

We next collected HDX-MS data on Trio₁₂₈₄₋₁₉₅₉, Rac1·GDP, and their complex to see if there were regions in the C terminus of the Trio fragment beyond the PH domain

Table 1
Cryo-EM data collection, processing, and model fitting statistics

Trio ₁₂₈₄₋₁₉₅₉ –Rac1 complex EMDB-25153 PDB 7SJ4	
Data collection and processing	
Magnification	81,000
Voltage (kV)	300
Electron exposure (e ⁻ /Å ²)	55
Defocus range (μm)	–0.5~–2.2
Pixel size (Å)	0.54
Symmetry imposed	C1
Initial particle images (no.)	2,066,058
Final particle images (no.)	922,202
Map resolution (Å)	2.86
FSC threshold	0.143
Refinement	
Initial model used (PDB code)	2NZ8
Model resolution (Å)	2.0
Map sharpening <i>B</i> factor (Å ²)	–147
Model composition	
Nonhydrogen atoms	3909
Protein residues	481
Water	24
<i>B</i> factors (Å ²)	
Protein	74.7
Ligand	46.1
R.m.s. deviations	
Bond lengths (Å)	0.002
Bond angles (°)	0.432
Validation	
MolProbity score	1.14
Clashscore	3.47
Poor rotamers (%)	0.93
Ramachandran plot	
Favored (%)	98.73
Allowed (%)	1.27
Disallowed (%)	0

whose dynamics changed upon complex formation, as one might expect if they interacted with either regions in the fragment or Rac1. The HDX-MS map of Trio₁₂₈₄₋₁₉₅₉ alone (Fig. S6) showed the anticipated exchange pattern for peptides derived from the DH and PH domains of the GEF module (residues 1284–1594), with lower exchanging regions corresponding to those observed in crystal structures and surface residues and loops displaying higher exchange. Following the GEF module, the only peptides showing any solvent protection are those roughly corresponding to the SH3N domain. The linker region we showed to confer activation (residues 1719–1959) are likely disordered because they all exchange within 10 s after the start of the experiment. The corresponding map for Rac1·GDP (Fig. S8A) was consistent with crystal structures of the molecule. In HDX-MS difference maps comparing Trio₁₂₈₄₋₁₉₅₉ and Rac1·GDP alone to the Trio₁₂₈₄₋₁₉₅₉–Rac1 complex (Figs. 5, 6 and S6–S8), the overall HDX profile is as one might expect from the structure of the TrioN–Rac1 complex. Residues from each protein that form the interface exhibited a decrease in exchange in the complex consistent with their sequestration from solvent, including Trio₁₂₈₄₋₁₉₅₉ residues in α 1, α 3, α 4, α 5, and most strongly α 6. Residues in switch 1 and switch 2 of Rac1 which form the binding surface and interact with the DH domain in Trio₁₂₈₄₋₁₉₅₉ also displayed lowered exchange rates in the complex, indicative of sequestration from solvent. On the other hand, Rac1 residues in β 1, α 1, β 5, α 4, and the β 6– α 6 loop which contact the nucleotide when bound exhibited an increase in exchange, consistent with an expected increase in dynamics associated with the nucleotide-free state of Rac1 when bound to the DH domain. Trio residues 1719–1959 showed no change in deuterium incorporation upon complex formation (Fig. 6), suggesting that residues in this region only transiently interact with Rac1 or the TrioN GEF module.

Analysis of Trio₁₂₈₄₋₁₉₅₉ enhanced activity using site-directed mutagenesis

Because we could not detect any region within residues 1595 to 1959 that might contribute to enhanced Rac1 GEF activity by TrioN by cryo-EM or HDX-MS, we assessed if there were spans of residues in this region that were conserved across metazoan life and found two prominent ones: a basic and hydrophobic motif and a proline-rich motif at Trio residues 1772 to 1784 and 1867 to 1873, respectively (Fig. 7A). We created and purified deletion variants of each span (Trio₁₂₈₄₋₁₉₅₉Δ1772-1784 and Trio₁₂₈₄₋₁₉₅₉Δ1867-1873) and compared their GEF activity against those of TrioN and Trio₁₂₈₄₋₁₉₅₉ (Fig. 7B). Deletion of either conserved span led to reduction of Rac1 GEF activity to the same level as that of TrioN, indicating that both elements are essential for the increased catalytic proficiency of Trio₁₂₈₄₋₁₉₅₉.

Discussion

We expected that learning more about Trio domains accessory to the GEF modules would provide details about

Structure/function studies of human Trio

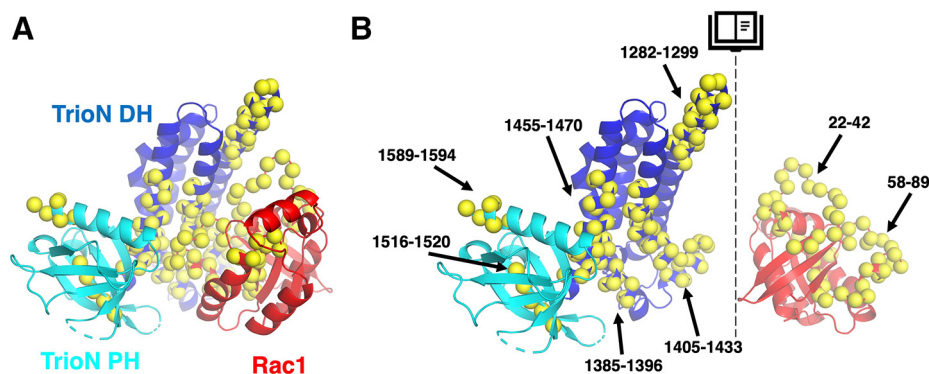


Figure 5. Mapping the interaction interface between Trio₁₂₈₄₋₁₉₅₉ and Rac1. *A*, location of decreased HDX signal in the complex structure of Trio₁₂₈₄₋₁₉₅₉-Rac1 modeled using the crystal structure of the TrioN-Rac1 complex (PDB 2NZ8). Ca positions of residues with decreased HDX signal are indicated with a yellow sphere. The DH and PH domains of TrioN are shown in blue and cyan, respectively. Rac1 is red. *B*, “open book” view of TrioN and Rac1 showing regions with decreased HDX signal, wherein both subunits in panel *A* have been rotated 90° in opposite directions around the vertical axis (dashed lines). DH, Dbl homology; HDX, hydrogen-deuterium exchange; GEF, guanine nucleotide exchange factor; PH, pleckstrin homology.

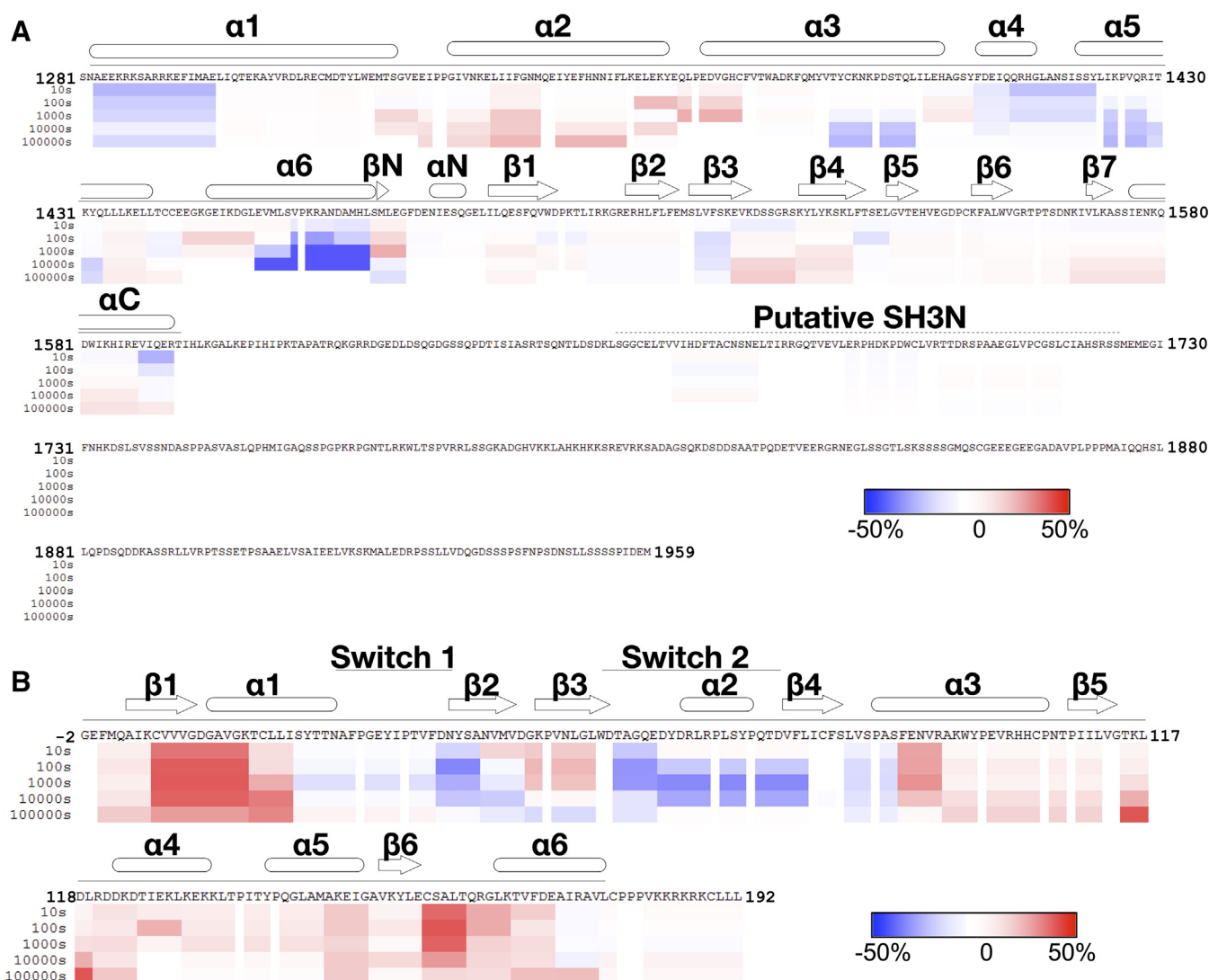


Figure 6. The HDX-MS profile of Trio₁₂₈₄₋₁₉₅₉ suggests that residues within the 1718 to 1959 region do not form a stable interaction with either Rac1 or TrioN. *A*, HDX-MS difference map of Trio₁₂₈₄₋₁₉₅₉ alone versus in complex with Rac1. *B*, HDX-MS difference maps of Rac1 alone versus in complex with Trio₁₂₈₄₋₁₉₅₉. The extent of deuterium incorporation is shown as colored rectangles, indicating less exchange (blue) to more exchange (red) of the complex relative to the isolated subunits. Time points are shown on the left in seconds. Protein primary sequences are shown with secondary structure above each profile, with a helices shown as rounded cylinders, β strands as arrows, and a straight line indicating ordered regions of the Trio₁₂₈₄₋₁₉₅₉-Rac1 cryo-EM structure. EM, electron microscopy; HDX-MS, hydrogen-deuterium exchange mass spectroscopy.

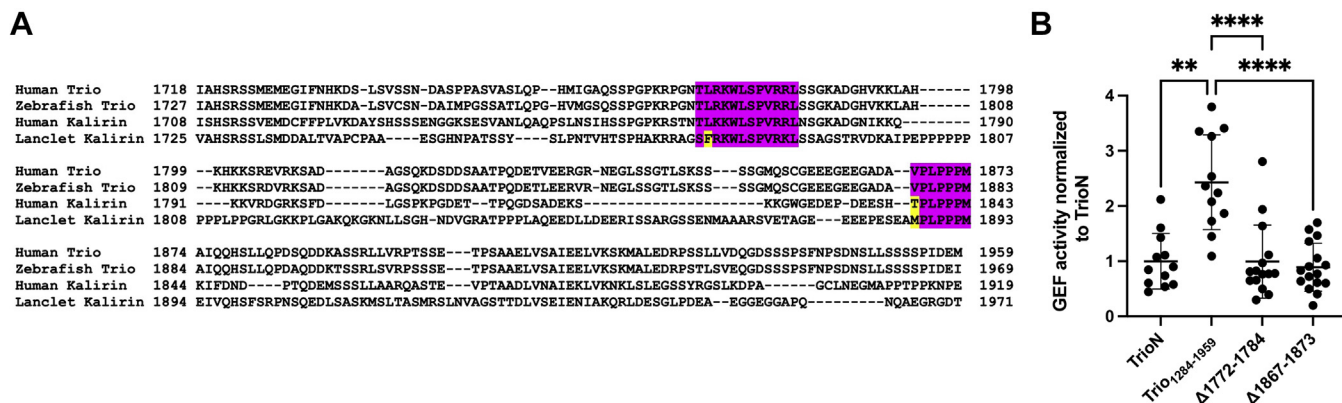


Figure 7. Identification of linker regions that contribute to GEF activity on TrioN. *A*, representative sequences from a multisequence alignment of Trio homologs and Kalirin orthologs. There are two conspicuous spans of residues that are highly conserved across the 13 vertebrate and invertebrate sequences analyzed (purple and yellow highlights corresponding to identical/highly conserved and conserved positions, respectively). Uniprot entries for the shown sequences are O75962 (human Trio Isoform1), F1Q551 (zebrafish Trio Isoform 1), O60229 (human Kalirin Isoform 1), and A0A6P4YL6 (amphioxus Kalirin). *B*, deletion of either conserved span decreased exchange on Rac1 to a level similar to TrioN alone. Each dot represents an individual experiment from $N = 12$ total experiments. Error bars indicate standard deviation. $^{**}p = 0.0045$; $^{****}p < 0.0001$.

autoregulation of GEF activity, thereby creating opportunities for discovery of therapeutics that selectively target these unique regulatory mechanisms. To this end, we characterized large Trio fragments using negative stain and cryo-EM, HDX-MS, and FRET-based nucleotide exchange assays. The N-terminal region of Trio (represented by Trio_{MBP-61-1594}), which is dominated by nine spectrin repeats, forms a particle with an extended conformation as visualized by negative stain EM (Fig. 1B). Thus, we speculate, as have others, that the spectrin repeats may serve to maintain distance between the domains present at each end, in this case a lipid or protein binding activity of the CT domain and the Rac1/RhoA exchange activity of TrioN (Fig. 8). Distance between a lipid binding site and GEF activity may be important in the neurite outgrowth process wherein the extension of neurites requires a particular distance between plasma membrane components and the actin cytoskeleton (28, 33). Indeed, Trio's involvement in neurite outgrowth requires the spectrin repeat region, TrioN GEF activity, and the SH3N domain (28). The extended spectrin repeat region may also provide a docking interface for other proteins such as supervillin (34). Higher resolution insights into this region by EM would however require somehow reducing conformational heterogeneity.

Conversely, the central region of Trio (residues 1284–2638) was globular in negative stain EM micrographs, but no high-resolution features were present in the resulting 2D averages, suggesting that this portion of Trio may consist of self-associating regions that are loosely organized, at least without other interaction partners. Consistent with this idea, we found that larger Trio constructs exhibited faster Rac1 exchange rates than the TrioN GEF module alone. Activated $G\alpha_q$ in the form of $G\alpha_q \bullet GDP \bullet AIF_4^-$ did not affect the Rac1 nucleotide exchange of any fragment tested (Figs. 2 and S3) but did activate fragments containing TrioC ~2.5-fold (Figs. 2 and S3). Thus, $G\alpha_q$ binding does not seem to allosterically affect TrioN GEF activity and allosterically activates the TrioC module regardless of its context. Because $G\alpha_q$ binding was

observed to stimulate both Rac1 and RhoA exchange *via* Trio in cells (6, 7), it seems likely that $G\alpha_q$ stimulates Rac1 turnover through Trio simply by driving the association of Trio to the plasma membrane where Rac1 and RhoA are localized (Fig. 7).

The minimum fragment required in our study to see significant Rac1 turnover rate enhancement spanned residues 1284 to 1959, including TrioN, SH3N, and a 240-residue low complexity linker that extends to the beginning of the TrioC module (Fig. 3). Because Trio₁₂₈₄₋₁₇₁₈ did not display enhanced exchange rate, we concluded that the 240-residue region between SH3N and TrioC (residues 1719–1959) was critical for rate enhancement. However, analysis of the Trio₁₂₈₄₋₁₉₅₉-Rac1 complex using cryo-EM did not find evidence for any ordered portion of the 1719 to 1959 region that might facilitate complex formation (Figs. 4–6). Furthermore, the 1719 to 1959 region exhibited high dynamics by HDX-MS regardless of Rac1 binding (Figs. 6A and S6 and S7). Thus, if elements within the 1719 to 1959 region directly facilitate GEF activity, it seems they only do so transiently. Sequence analysis of Trio and its close ortholog Kalirin across vertebrates and invertebrates reveal two highly conserved spans in the 1719 to 1959 region (Fig. 7A). Deletion of either span eliminated enhancement of GEF activity by Trio₁₂₈₄₋₁₉₅₉, indicating that they may be playing evolutionarily important roles, but the underlying mechanisms remain unknown. One span (1772–1784) is both basic and hydrophobic and may transiently interact with a complementary region on TrioN or Rac1. The other conserved span (1867–1873) is proline rich and contains a PXXP motif, suggesting that it could bind to one (or both) SH3 domains in Trio. A peptide corresponding to the analogous span was tested for binding to SH3N in Kalirin, but its affinity was much weaker than other PXXP containing peptides tested from the N-terminal half of the enzyme. Furthermore, the interaction of these peptides with SH3N was reported to be inhibitory toward GEF activity (26). We did not detect an analogous decrease in GEF activity when comparing TrioN to longer fragments also containing the

Structure/function studies of human Trio

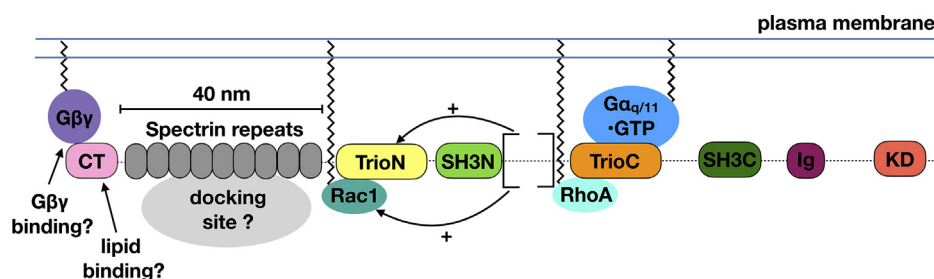


Figure 8. Hypotheses for Trio regulation. From left to right, the CT domain may interact with $G\beta\gamma$ or specific lipids on the plasma membrane and cooperate with the spectrin region to spatially regulate Rac1 signaling. The spectrin repeat region may also serve as a docking site for other signaling proteins or complexes. The 1718 to 1959 region following the SH3N domain (bracketed) facilitates nucleotide exchange on Rac1 via a transient interaction with either TrioN, Rac1, or SH3N. $G\alpha_{q/11}$ binds to the TrioC module to directly enhance RhoA nucleotide exchange and likely helps to localize Trio to the plasma membrane, which in turn enhances Rac1 exchange as observed in cells. *Serrated lines* represent lipid modifications, and *dashed lines* represent putative unstructured regions (not drawn to scale). CT, Cral/Trio.

SH3N domain. Instead, we documented profoundly higher activity. Whether the SH3N domain is required for this boost in GEF activity in Trio is not yet known. Our opposing results from those reported for Kalirin could be due to distinct experimental conditions and/or different protein fragments being tested (or even a fundamental difference between Kalirin and Trio). Regardless, both sets of data suggest that there exist complex intramolecular interactions mediated by various motifs within the low complexity linker regions in these proteins which likely contribute to spatial and temporal regulation of Trio in cells. These interactions present an opportunity to modulate Trio function for therapeutic benefit.

Experimental procedures

Cloning

Human Trio cDNA consisting of a DNA sequence corresponding to residues 61 to 3097 in pcDNA3.1 was described previously (7). All Trio protein constructs are described with numbering relative to isoform 1 in UniProt entry O75962 and were designed using insight from the XtalPred Server (35) and Clustal Omega (36). DNA regions for larger Trio constructs were amplified using the KOD polymerase kit (EMD Millipore) following manufacturer's instructions, which was necessary for productive high-fidelity amplification. Individual Trio domains were amplified using Q5 polymerase (NEB). Deletions were generated using overlap extension PCR. Inserts were generated using PCR reactions with ligation-independent cloning handles on 5' and 3' ends, purified using a PCR cleanup kit (Qiagen), and inserted into the pMCSG9 vector using the ligation-independent cloning protocol (37). This allowed for *E. coli* expression and affinity purification of MBP-Trio fusion variants (N-6xHis-MBP-TEV-Trio-C). Constructs were confirmed using Sanger sequencing of plasmid DNA purified using a Mini-prep kit (Qiagen). The RhoA and Rac1 constructs were described previously (38) and consist of residues 1 to 193 of human RhoA and 1 to 192 of human Rac1. The $G\alpha_q$ construct used was also described previously (39).

Protein expression and purification

RhoA and Rac1 were purified as described (38). Plasmids encoding Trio variants were transformed into Rosetta (DE3)

pLysS *E. coli* cells (Novagen) and grown in terrific broth (EMD Millipore Sigma) with 100 $\mu\text{g}/\text{ml}$ ampicillin or carbenicillin plus 50 $\mu\text{g}/\text{ml}$ chloramphenicol at 37 °C with 200 rpm shaking. Once an A_{600} of 0.6 to 0.8 was reached, expression of N-terminally tagged fusion proteins was induced using 0.5 mM isopropyl β -D-1-thiogalactopyranoside, and cells were transferred to 20 °C with 200 rpm shaking for 20 to 24 h. Cells were then harvested at 5000g for 15 min, and cell pellets were flash-frozen if not immediately prepared. Cell pellets were vortexed and resuspended using a dounce homogenizer in ice-cold lysis buffer consisting of 20 mM 4-(2-hydroxyethyl)-1-piperazineethanesulfonic acid (HEPES) pH 8.0, 200 mM NaCl, 2 mM dithiothreitol (DTT), 5% (v/v) glycerol, 0.001 mM leupeptin, 1 mM lima bean trypsin inhibitor, 0.1 mM phenylmethylsulfonyl fluoride, and 5 mM EDTA. Resuspended cell solution was then lysed using a handheld VirSonic 100 Sonicator (Boston Laboratory Equipment) for five 30-s pulses at 18 W on ice. Lysate was then centrifuged at 40,000 rpm in a Beckman Optima L-90K ultracentrifuge (Beckman-Coulter) to remove insoluble material. The soluble fraction was then filtered through a 0.45 μm filter and loaded onto Roche cComplete His-tag resin (Roche 5893682001) equilibrated with lysis buffer. Two aliquots of 10 column volumes of lysis buffer containing 10 mM imidazole were used to wash the column. The recombinant protein was then eluted using lysis buffer plus 200 mM imidazole. The elution fractions containing the desired protein were then incubated with 5% (w/w) tobacco etch virus protease to cleave the N-terminal expression tag, and the mixture was dialyzed against a buffer containing 20 mM HEPES pH 8.0, 200 mM NaCl, and 2 mM DTT. After removal of the MBP fragment by passage through a cComplete resin column, Trio constructs were dialyzed against 20 mM HEPES pH 8.0, 10 mM NaCl, and 2 mM DTT overnight at 4 °C. Proteins were subjected to anion exchange chromatography using a 5 ml HiTrap Q HP column (GE 17115401) using a buffer of 20 mM HEPES pH 8.0 and 2 mM DTT with a gradient of 10 mM to 1000 mM NaCl over 100 ml. Desired fractions were concentrated in a 30 or 50 kDa cutoff concentrator and loaded on either a 24 ml Superose 6 or a Superdex 200 column (GE) equilibrated with 20 mM HEPES pH 8.0, 200 mM NaCl, and 2 mM DTT. Desired fractions from SEC were concentrated to 1 to 2 mg/ml and flash frozen in

liquid N₂. For formation of Trio–GTPase complexes, Trio variants were mixed with >2-fold molar excess of GTPase in a buffer containing 0.1 mM EDTA to drive complex formation. Complexes were incubated at 4 °C for >30 min and then loaded on an S200 column equilibrated with 20 mM HEPES pH 8.0, 200 mM NaCl, 2 mM DTT, and 0.1 mM EDTA. Fractions containing complex were concentrated in a 30 kDa cutoff concentrator, and protein concentration was determined using A₂₈₀.

Negative stain EM data collection and processing

Negative staining of Trio samples was performed similarly to that previously described (40). Purified protein samples were applied to a glow discharged formvar coated copper grid (Electron Microscopy Sciences FCF400-Cu-50) for 1 min. Grids were first blotted against filter paper, then processed by two rounds of dipping into ddH₂O followed by blotting, and then two rounds of dipping into 0.75% (w/v) uranyl formate stain followed by blotting. The grids were then dipped into another drop of stain for 1 min. Finally, grids were blotted dry and dried using a vacuum line. The resulting grids were evaluated for stain quality, contrast, particle quality, and particle spread using a Morgagni 100 kV transmission electron microscope (TEM). Micrographs were collected on it using a CCD camera at 2.1 Å/pixel at a nominal magnification of 22,000× using an exposure time of 1 s. Optimal grids were taken for further imaging on the Tecnai T12 120 kV TEM operated using the Legicon automated data collection system (41) and a nominal magnification of 67,000×, 1 s exposure time, and a CCD camera at 1.68 Å/pixel. Particles were picked for 2D class averaging using the *cis*TEM software suite (42). For the Trio₁₂₈₄₋₂₆₃₈ construct, 4000 particles were averaged into 20 classes. For the Trio₁₂₈₄₋₁₉₅₉–Rac1 complex, 15,000 particles were averaged into 50 classes. Use of fewer classes for the Trio₁₂₈₄₋₁₉₅₉–Rac1 complex did not improve detail.

FRET-based guanine exchange factor assay

FRET was used to assess the nucleotide exchange activity of Trio variants (13, 43). In a 384-well black low-volume round-bottom microplate (Corning 4514), 2 μM RhoA-GDP or Rac1-GDP was incubated with 50 nM GEF for 5 min at room temperature in freshly prepared nucleotide exchange buffer containing 20 mM HEPES pH 8.0, 200 mM NaCl, 2 mM DTT, and 10 mM MgCl₂. Immediately before measurement, 1 μM 2/3'-O-(N-methyl-anthraniloyl)-guanosine-5'-triphosphate (MANT-GTP) (Jena Biosciences) was added to a final assay volume of 20 μl. The mixture was then excited at 280 nm, and fluorescence emission at 450 nm was read in 5 s intervals on a SpectraMax M5 plate reader (Molecular Devices) for 5 to 10 min. Resulting curves were fit to a linear regression model to derive the observed kinetic constant *k*_{obs} and then compared to that of matched rates of GTPase alone and GTPase + control GEF (TrioN or TrioC). For Gα_q activation assays, Gα_q-GDP was added at 200 nM, and the assay was run in the presence or absence of 30 μM AlCl₃ and 10 mM NaF, which generates the active Gα_q-GDP·AlF₄⁻ complex. For GEF assays shown in Figure 7B, the protocol is same as

mentioned above except the fluorescence curves were measured on a Flexstation 3 plate reader (Molecular Devices) and fitted to a one-phase exponential association model ($Y=Y_0 + \text{SPAN}^*(1 - \exp(-k*X))$) with SPAN constrained to be shared for all datasets in a single experiment.

Statistical analysis

FRET nucleotide exchange assays were performed in at least three independent experiments. For assays in Figures 2 and S3, the three experiments were performed using aliquots from the same protein preparation. For assays in Figure 3, the first experiment was performed using one protein preparation, the second and third were performed using protein from a second purification. For assays comparing basal GEF activities in Figures 2 and 3, *k*_{obs} values were normalized to rate of GTPase alone to generate fold activation values for each variant. For Gα_q-GDP·AlF₄⁻ activation assays in Figure 2B, *k*_{obs} values were normalized to rate of GTPase alone to generate fold activation values for each. For GEF assays shown in Figure 7B, FRET experiments were performed with protein from single preparations of TrioN and Trio₁₂₈₄₋₁₉₅₉ as negative and positive controls, respectively, but two different preparations of each deletion mutant. These assays were normalized to the rate of Rac1 + TrioN, and Fig. S3 were normalized to the rate of GTPase + GEF + Gα_q-GDP (no AlF₄⁻ added). Statistical significance was assessed using a one-way ANOVA test with a post-hoc Dunnett's test for multiple comparisons. In basal GEF assays, each Trio variant is statistically compared to either TrioN or TrioC. Normalized *k*_{obs} in the presence of Gα_q-GDP·AlF₄⁻ for each variant was statistically compared to *k*_{obs} in the presence of Gα_q-GDP. Errors are presented as standard deviations from the mean. Analyses were performed using GraphPad Prism, version 7.0.

Hydrogen-deuterium exchange mass spectrometry

HDX-MS experiments were carried out as previously described (13). The optimal quench solution to give best sequence coverage map of the Trio₁₂₈₄₋₁₉₅₉–Rac1 complex contained 6.4 M guanidinium hydrochloride (Gu-HCl), 1 M Tris(2-carboxyethyl)phosphine, and 0.1 M glycine, pH 2.4. All exchange stock solutions were prepared on ice and contained 2.5 mg/ml of Trio₁₂₈₄₋₁₉₅₉, 2.5 mg/ml of Trio₁₂₈₄₋₁₉₅₉–Rac1, and 2.2 mg/ml of Rac1 in 8.3 mM Tris pH 7.2 and 150 mM NaCl. The exchange experiments were initiated by adding 2 μl of stock solutions to 4 μl of D₂O buffer containing 8.3 mM Tris, 150 mM NaCl, pH 7.2. The exchange solutions were kept at 0 °C for 10, 100, 1,000, 10,000, and 100,000 s and then quenched by the addition of 9 μl of the quench solution and incubated on ice for 10 min. The quenched samples were further diluted with 45 μl of 0.1 M glycine, pH 2.4, 16.6% (v/v) glycerol to drop the Gu-HCl concentration below 1 M and stored on dry ice. All samples were passed through a pepsin column for enzymatic digestion, and the resulting peptides were collected on a trap column (Optimize Tech, OptiTrap, 0.2 × 2 mm). Liquid chromatography separations were performed on an Agilent C18 column (Poroshell 120, 0.3 × 35 mm, 2.7 μm) with a linear acetonitrile gradient and analyzed using an Orbitrap Elite Mass Spectrometer (Thermo Fisher Scientific), which was tuned

Structure/function studies of human Trio

up for HDX experiments (44). Data acquisition and peptide identification were done by Xcalibur 3.0 and Proteome Discoverer 1.3 (Thermo Fisher Scientific). Deuterium uptake was calculated with HDXaminer (Sierra Analytics, LLC), by correcting the back-exchange with control samples. Ribbon map coloring were generated using MATLab by combining deuterium uptake information of overlapping peptides.

Cryo-EM data collection and processing

The Trio₁₂₈₄₋₁₉₅₉-Rac1 complex was prepared at 2.6 μM concentration and n-dodecyl-β-D-maltoside was added to a final concentration of 0.08 mM. Samples were frozen using the Vitrobot automated grid freezing system (FEI) on UltraAuFoil R (1.2/1.3) 300-mesh gold grids (Electron Microscopy Sciences). The Vitrobot was set to 4 °C, 100% humidity, 3.5 s blot, and a force of 10. Cryo-EM samples were screened using the 200 kV Talos F200C Glacios TEM, and grids with evenly distributed particles were clipped using C-clips (Electron Microscopy Sciences) for the following cryo-EM data collection using the 300 kV Titan Krios G1 TEM with a post-GIF K3 direct electron detector at 0.54 Å/pixel with a nominal magnification of 81,000×. Each of the 3514 movies collected has 40 consecutive frames, which were used to generate a motion-corrected micrograph by MotionCor2 (45). The contrast transfer function (CTF) of each micrograph was estimated using the Patch-CTF estimation package in cryoSPARC with default settings. After rejection of micrographs with poor CTF fitting, 2817 micrographs were used for particle picking and extraction using cryoSPARC (46). Successive rounds of reference-free 2D classification were performed to select protein particles while eliminating junk particles, yielding 1,216,361 particles. After application of the Rebalance 2D step, 904,361 particles were selected for producing two *ab initio* models, which were used to classify the 1,216,361 particles in the 3D heterogeneous refinement. Finally, 922,202 particles were used for homogenous refinement to obtain a 3D map. Two reconstructed half maps were used for resolution estimation using the Fourier shell correlation criterion of 0.143, and a sharpened map was used for model building in RELION (47). The crystal structure of the N-terminal DH/PH cassette of TrioN complexed with Rac1¹⁶ (PDB: 2NZ8) was first rigid-body fit into the cryo-EM map using UCSF Chimera (48) and subjected to manual model building and real-space refinement using Coot (49) and PHENIX (50). Model validation was performed by MolProbity (51). Coordinates and maps were deposited in the PDB as entry 7SJ4 and the EMDB as entry 25153.

Data availability

Plasmids and other reagents are available upon reasonable request to J. J. G. T. The model for the Trio₁₂₈₄₋₁₉₅₉-Rac1 complex has been deposited as PDB entry 7SJ4 and as EMDB entry EMD-25153.

Supporting information—This article contains supporting information.

Acknowledgments—We thank the lab of Dr Janet Smith and the Life Sciences Institute (LSI) High-Throughput Protein Lab for valuable discussion regarding cloning, and the LSI for use of the SpectraMax M5 plate reader. We thank Dr Veronica Taylor for supplying purified Gα_q. We also thank Drs Min Su and Amy Bondy of the LSI electron microscopy facility for training. We finally thank Dr Michael Cianfrocco for advice and valuable discussion on EM data collection and processing.

Author contributions—S. J. B. and J. J. G. T. conceptualization; S. J. B. and J. J. G. T. methodology; S. J. B., J. S. G., and J. J. G. T. funding acquisition; S. J. B., C-L. C., S. K. R., S. L., L. V. A., and M. V. Z., investigation; S. J. B., J. N. C., C-L. C., and S. L., data curation; S. J. B. writing-original draft; S. J. B., S. L., C-L. C., J. N. C., S. K. R., J. S. G., and J. J. G. T. writing-review & editing.

Funding and additional information—This work was supported by the National Institutes of Health grants CA221289, HL071818, and CA254402 (to J. J. G. T.) and F31CA224804 (to S. J. B.). The content is solely the responsibility of the authors and does not necessarily represent the official views of the National Institutes of Health.

Conflict of interest—The authors declare that they have no conflicts of interest with the contents of this article.

Abbreviations—The abbreviations used are: CT, Cral/Trio; DH, Db1 homology; EM, electron microscopy; FRET, Förster resonance energy transfer; GEF, guanine nucleotide exchange factor; HDX-MS, hydrogen-deuterium exchange mass spectrometry; MBP, maltose binding protein; PH, pleckstrin homology; RhoGEFs, Rho family guanine nucleotide exchange factors; SH3N, N-terminal Src homology 3 domain; SH3C, C-terminal Src homology 3 domain; TrioN, N-terminal GEF module; TrioC, C-terminal GEF module.

References

1. Rossman, K. L., Der, C. J., and Sondek, J. (2005) GEF means go: turning on RHO GTPases with guanine nucleotide-exchange factors. *Nat. Rev. Mol. Cell Biol.* **6**, 167–180
2. Bar-Sagi, D., and Hall, A. (2000) Ras and rho GTPases: a family reunion. *Cell* **103**, 227–238
3. Cook, D. R., Rossman, K. L., and Der, C. J. (2014) Rho guanine nucleotide exchange factors: regulators of Rho GTPase activity in development and disease. *Oncogene* **33**, 4021–4035
4. Vega, F. M., and Ridley, A. J. (2008) Rho GTPases in cancer cell biology. *FEBS Lett.* **582**, 2093–2101
5. Schmidt, S., and Debant, A. (2014) Function and regulation of the Rho guanine nucleotide exchange factor Trio. *Small GTPases* **5**, e29769
6. Feng, X., Degese, M. S., Iglesias-Bartolome, R., Vaque, J. P., Molinolo, A. A., Rodrigues, M., *et al.* (2014) Hippo-independent activation of YAP by the GNAQ uveal melanoma oncogene through a Trio-regulated rho GTPase signaling circuitry. *Cancer Cell* **25**, 831–845
7. Vaque, J. P., Dorsam, R. T., Feng, X., Iglesias-Bartolome, R., Forsthoefel, D. J., Chen, Q., *et al.* (2013) A genome-wide RNAi screen reveals a Trio-regulated Rho GTPase circuitry transducing mitogenic signals initiated by G protein-coupled receptors. *Mol. Cell* **49**, 94–108
8. Carvajal, R. D., Piperno-Neumann, S., Kapiteijn, E., Chapman, P. B., Frank, S., Joshua, A. M., *et al.* (2018) Selumetinib in combination with dacarbazine in patients with metastatic uveal melanoma: a phase III, multicenter, randomized trial (SUMIT). *J. Clin. Oncol.* **36**, 1232–1239
9. Mallone, F., Sacchetti, M., Lambiase, A., and Moramarco, A. (2020) Molecular insights and emerging strategies for treatment of metastatic uveal melanoma. *Cancers (Basel)* **12**, 2761

10. Yoshizuka, N., Moriuchi, R., Mori, T., Yamada, K., Hasegawa, S., Maeda, T., *et al.* (2004) An alternative transcript derived from the Trio locus encodes a guanosine nucleotide exchange factor with mouse cell-transforming potential. *J. Biol. Chem.* **279**, 43998–44004
11. Skowronek, K. R., Guo, F., Zheng, Y., and Nassar, N. (2004) The C-terminal basic tail of RhoG assists the guanine nucleotide exchange factor Trio in binding to phospholipids. *J. Biol. Chem.* **279**, 37895–37907
12. Chhatiwala, M. K., Betts, L., Worthylake, D. K., and Sondek, J. (2007) The DH and PH domains of Trio coordinately engage Rho GTPases for their efficient activation. *J. Mol. Biol.* **368**, 1307–1320
13. Bandekar, S. J., Arang, N., Tully, E. S., Tang, B. A., Barton, B. L., Li, S., *et al.* (2019) Structure of the C-terminal guanine nucleotide exchange factor module of Trio in an autoinhibited conformation reveals its oncogenic potential. *Sci. Signal.* **12**, eaav2449
14. Schmidt, S., Diriong, S., Mery, J., Fabbriozzi, E., and Debant, A. (2002) Identification of the first Rho-GEF inhibitor, TRIPalpha, which targets the RhoA-specific GEF domain of Trio. *FEBS Lett.* **523**, 35–42
15. Bouquier, N., Fromont, S., Zeeh, J. C., Auziol, C., Larrousse, P., Robert, B., *et al.* (2009) Aptamer-derived peptides as potent inhibitors of the oncogenic RhoGEF Tgat. *Chem. Biol.* **16**, 391–400
16. Gray, J. L., von Delft, F., and Brennan, P. E. (2020) Targeting the small GTPase superfamily through their regulatory proteins. *Angew. Chem.* **59**, 6342–6366
17. Aittaleb, M., Boguth, C. A., and Tesmer, J. J. (2010) Structure and function of heterotrimeric G protein-regulated rho guanine nucleotide exchange factors. *Mol. Pharmacol.* **77**, 111–125
18. Kim, K., Lee, J., Lee, S. A., Moon, H., Park, B., Kim, D., *et al.* (2017) Intermolecular steric inhibition of Ephexin4 is relieved by Elmo1. *Sci. Rep.* **7**, 4404
19. Mitin, N., Betts, L., Yohe, M. E., Der, C. J., Sondek, J., and Rossman, K. L. (2007) Release of autoinhibition of ASEF by APC leads to CDC42 activation and tumor suppression. *Nat. Struct. Mol. Biol.* **14**, 814–823
20. Soykan, T., Schneeberger, D., Tria, G., Buechner, C., Bader, N., Svergun, D., *et al.* (2014) A conformational switch in collybistin determines the differentiation of inhibitory postsynapses. *EMBO J.* **33**, 2113–2133
21. Bankaitis, V. A., Mousley, C. J., and Schaaf, G. (2010) The Sec14 superfamily and mechanisms for crosstalk between lipid metabolism and lipid signaling. *Trends Biochem. Sci.* **35**, 150–160
22. Aravind, L., Neuwald, A. F., and Ponting, C. P. (1999) Sec14p-like domains in NF1 and Dbl-like proteins indicate lipid regulation of Ras and Rho signaling. *Curr. Biol.* **9**, R195–R197
23. Nishida, K., Kaziro, Y., and Satoh, T. (1999) Association of the proto-oncogene product dbl with G protein betagamma subunits. *FEBS Lett.* **459**, 186–190
24. Djinic-Carugo, K., Gautel, M., Ylanne, J., and Young, P. (2002) The spectrin repeat: a structural platform for cytoskeletal protein assemblies. *FEBS Lett.* **513**, 119–123
25. Kaneko, T., Li, L., and Li, S. S. (2008) The SH3 domain—a family of versatile peptide- and protein-recognition module. *Front. Biosci.* **13**, 4938–4952
26. Schiller, M. R., Chakrabarti, K., King, G. F., Schiller, N. I., Eipper, B. A., and Maciejewski, M. W. (2006) Regulation of RhoGEF activity by intramolecular and intermolecular SH3 domain interactions. *J. Biol. Chem.* **281**, 18774–18786
27. Medley, Q. G., Serra-Pages, C., Iannotti, E., Seipel, K., Tang, M., O'Brien, S. P., *et al.* (2000) The Trio guanine nucleotide exchange factor is a RhoA target. Binding of RhoA to the Trio immunoglobulin-like domain. *J. Biol. Chem.* **275**, 36116–36123
28. Estrach, S., Schmidt, S., Diriong, S., Penna, A., Blangy, A., Fort, P., *et al.* (2002) The Human Rho-GEF Trio and its target GTPase RhoG are involved in the NGF pathway, leading to neurite outgrowth. *Curr. Biol.* **12**, 307–312
29. Rojas, R. J., Yohe, M. E., Gershuberg, S., Kawano, T., Kozasa, T., and Sondek, J. (2007) Galphaq directly activates p63RhoGEF and Trio via a conserved extension of the Dbl homology-associated pleckstrin homology domain. *J. Biol. Chem.* **282**, 29201–29210
30. Lutz, S., Shankaranarayanan, A., Coco, C., Ridilla, M., Nance, M. R., Vettel, C., *et al.* (2007) Structure of $G\alpha_q$ -p63RhoGEF-RhoA complex reveals a pathway for the activation of RhoA by GPCRs. *Science* **318**, 1923–1927
31. Williams, S. L., Lutz, S., Charlie, N. K., Vettel, C., Ailion, M., Coco, C., *et al.* (2007) Trio's Rho-specific GEF domain is the missing $G\alpha_q$ effector in *C. elegans*. *Genes Dev.* **21**, 2731–2746
32. Ortega, E., Manso, J. A., Buey, R. M., Carballido, A. M., Carabias, A., Sonnenberg, A., *et al.* (2016) The structure of the plakin domain of plectin reveals an extended rod-like shape. *J. Biol. Chem.* **291**, 18643–18662
33. Miller, K. E., and Suter, D. M. (2018) An integrated cytoskeletal model of neurite outgrowth. *Front. Cell Neurosci.* **12**, 447
34. Son, K., Smith, T. C., and Luna, E. J. (2015) Supravillin binds the Rac/Rho-GEF Trio and increases Trio-mediated Rac1 activation. *Cytoskeleton (Hoboken)* **72**, 47–64
35. Slabinski, L., Jaroszewski, L., Rychlewski, L., Wilson, I. A., Lesley, S. A., and Godzik, A. (2007) XtalPred: a web server for prediction of protein crystallizability. *Bioinformatics* **23**, 3403–3405
36. Sievers, F., and Higgins, D. G. (2021) The clustal omega multiple alignment package. *Met. Mol. Biol.* **2231**, 3–16
37. Brown, W. C., DelProposto, J., Rubin, J. R., Lamiman, K., Carless, J., and Smith, J. L. (2011) New ligation-independent cloning vectors compatible with a high-throughput platform for parallel construct expression evaluation using baculovirus-infected insect cells. *Protein Expr. Purif.* **77**, 34–45
38. Kristelly, R., Gao, G., and Tesmer, J. J. (2004) Structural determinants of RhoA binding and nucleotide exchange in leukemia-associated Rho guanine-nucleotide exchange factor. *J. Biol. Chem.* **279**, 47352–47362
39. Taylor, V. G., Bommarito, P. A., and Tesmer, J. J. (2016) Structure of the regulator of G protein signaling 8 (RGS8)-Galphaq complex: molecular basis for Galpha selectivity. *J. Biol. Chem.* **291**, 5138–5145
40. Ohi, M., Li, Y., Cheng, Y., and Walz, T. (2004) Negative staining and image classification - powerful tools in modern electron microscopy. *Biol. Proced. Online* **6**, 23–34
41. Carragher, B., Kisseberth, N., Kriegman, D., Milligan, R. A., Potter, C. S., Pulokas, J., *et al.* (2000) Leginon: an automated system for acquisition of images from vitreous ice specimens. *J. Struct. Biol.* **132**, 33–45
42. Grant, T., Rohou, A., and Grigorieff, N. (2018) cisTEM, user-friendly software for single-particle image processing. *Elife* **7**, e35383
43. Brecht, M., Sewald, K., Schiene, K., Keen, G., Fricke, M., Sauer, M., *et al.* (2004) The use of surface plasmon resonance (SPR) and fluorescence resonance energy transfer (FRET) to monitor the interaction of the plant G-proteins Ms-Rac1 and Ms-Rac4 with GTP. *J. Biotechnol.* **112**, 151–164
44. Walters, B. T., Ricciuti, A., Mayne, L., and Englander, S. W. (2012) Minimizing back exchange in the hydrogen exchange-mass spectrometry experiment. *J. Am. Soc. Mass Spectrom.* **23**, 2132–2139
45. Zheng, S. Q., Palovcak, E., Armache, J. P., Verba, K. A., Cheng, Y., and Agard, D. A. (2017) MotionCor2: anisotropic correction of beam-induced motion for improved cryo-electron microscopy. *Nat. Met.* **14**, 331–332
46. Punjani, A., Rubinstein, J. L., Fleet, D. J., and Brubaker, M. A. (2017) cryoSPARC: algorithms for rapid unsupervised cryo-EM structure determination. *Nat. Met.* **14**, 290–296
47. Zivanov, J., Nakane, T., Forsberg, B. O., Kimanius, D., Hagen, W. J., Lindahl, E., *et al.* (2018) New tools for automated high-resolution cryo-EM structure determination in RELION-3. *Elife* **7**, e42166
48. Pettersen, E. F., Goddard, T. D., Huang, C. C., Couch, G. S., Greenblatt, D. M., Meng, E. C., *et al.* (2004) UCSF Chimera—a visualization system for exploratory research and analysis. *J. Comput. Chem.* **25**, 1605–1612
49. Emsley, P., and Cowtan, K. (2004) Coot: model-building tools for molecular graphics. *Acta Crystallogr. D Biol. Crystallogr.* **60**, 2126–2132
50. Adams, P. D., Afonine, P. V., Bunkoczi, G., Chen, V. B., Davis, I. W., Echols, N., *et al.* (2010) Phenix: a comprehensive python-based system for macromolecular structure solution. *Acta Crystallogr. D Biol. Crystallogr.* **66**, 213–221
51. Chen, V. B., Arendall, W. B., 3rd, Headd, J. J., Keedy, D. A., Immormino, R. M., Kapral, G. J., *et al.* (2010) MolProbity: all-atom structure validation for macromolecular crystallography. *Acta Crystallogr. D Biol. Crystallogr.* **66**, 12–21